AIMS Materials Science, 11(6): 1065–1082.
DOI: 10.3934/matersci.2024051
Received: 20 September 2024
Revised: 21 October 2024
Accepted: 01 November 2024
Published: 07 November 2024

https://www.aimspress.com/journal/Materials

Research article

Green synthesis of high-performance gallium oxide supercapacitor: A path to outstanding energy density

Jamal Alnofiay[1,2], Ahmed Al-Shahrie[1] and Elsayed Shalaan[1,*]

[1] Department of Physics, Faculty of Science, King Abdulaziz University, Jeddah, 21589, Saudi Arabia
[2] Department of Physics, Faculty of Science, Taif University, Taif, 21944, Saudi Arabia

* **Correspondence:** Email: eshalan@kau.edu.sa; eshalaan@yahoo.com; Tel: +966-54-594-9570.

Abstract: Gallium oxide (Ga_2O_3) powder was prepared by mixing hydrogen peroxide (30% H_2O_2) with pure gallium metal (99.999%) inside a hydrothermal cell. The resulting white powder was subjected to different characterization techniques. X-ray diffraction (XRD) revealed the presence of multiple crystalline phases of gallium oxide, including monoclinic β-Ga_2O_3, and rhombohedral α-Ga_2O_3, as well as gallium suboxide Ga_2O. X-ray photoelectron spectroscopy (XPS) divulged Ga^{3+} as the dominant oxidation state of gallium in Ga_2O_3. However, a lower oxidation state, Ga^{1+}, was also detected. Scanning electron microscopy (SEM) images showed a high degree of morphological diversity with a wide variety in shape and size of powder particles. Porosity measurements were performed to determine the total surface area, pore diameter, and pore volume of Ga_2O_3 powder. The values were found to be 50 $m^2\ g^{-1}$, 2.6 nm, and 0.07 $cm^3\ g^{-1}$, respectively. Fascinatingly, gallium oxide powder was directly used to fabricate a symmetrical supercapacitor without any binder. Cyclic voltammetry (CV) and galvanostatic charge/discharge (GCD) measurements were performed to examine the electrochemical energy storage capabilities of Ga_2O_3 powder using 1M KOH as electrolyte. The fabricated supercapacitor demonstrated a maximum specific capacitance of 1176 F g^{-1}, at a current density of 2 A g^{-1}, an energy density of 104.5 Wh kg^{-1}, and a high-power density of 1.6 kW kg^{-1}. Additionally, following 5000 charge-discharge cycles, the supercapacitor demonstrated outstanding capacitance retention stability of 91.18%. The obtained energy density of 104.5 Wh kg^{-1} is among the highest reported for metal oxide-based supercapacitors. The presence of multiple crystalline phases in the gallium oxide powder likely contributed significantly to the remarkable results observed in this study.

Keywords: gallium oxide; supercapacitor; cyclic voltammetry; energy storage

1. Introduction

Supercapacitors are attracting significant attention due to their ability to bridge the gap between conventional capacitors and batteries. Distinctive features of supercapacitors include high energy density, fast charge and discharge rates, as well as extended cycle life. They are widely viewed as a very promising solution for energy storage, despite their lower energy density compared to batteries. The issue of low energy density is a limitation to their extensive use in energy storage applications.

The use of metal oxides, with their diverse electrochemical properties associated with faradaic processes, is a promising way to achieve high energy density [1,2]. There are two well-established oxides for supercapacitors, with ruthenium dioxide (RuO_2) being the most extensively studied pseudocapacitive material. It features high specific capacitance, good cycle stability, and exceptional rate capability. Although ruthenium dioxide is widely recognized as the material of choice for supercapacitor devices due to its high theoretical specific capacitance value of (1400–2000 F g^{-1}), its high production cost and agglomeration effects pose significant obstacles to commercial deployment [3,4]. Reported specific capacitance values for RuO_2 supercapacitors vary widely, ranging from about 80 F g^{-1} to more than 700 F g^{-1} [5–7]. Furthermore, the scarcity of ruthenium as a metal limits its widespread use in supercapacitors.

Manganese dioxide (MnO_2) is another commonly used pseudocapacitive material due to its low cost, environmental compatibility and accessibility. Likewise, while MnO_2 shows a high theoretical specific capacitance of about 1370 F g^{-1}, achieving this theoretical capacity in practical is difficult [8–10]. MnO_2 faces challenges such as low electrical conductivity, which hinders efficient charge transfer within the electrode, resulting in a decrease in overall capacitance. Furthermore, MnO_2 may experience a decrease in capacitance during charge-discharge cycles. Therefore, the specific capacitances obtained for MnO_2 electrodes are usually much lower than the theoretical value, ranging 250–400 F g^{-1} [10,11]. Although MnO_2 has not reached its theoretical peak in real-world applications, it remains a valuable material for supercapacitors due to its low cost, abundance, and potential for further improvements.

Accordingly, other metal oxides have been studied as potential materials for supercapacitors such as: NiO [12,13], SnO_2 [14,15], Bi_2O_3 [16], and $CoMoO_4$ [17–21]. Although these metal oxides show good energy storage performances, unfortunately they suffer from unacceptable physical and chemical properties coupled with complex manufacturing process which prevent them from being well commercialized. Hence, it is highly desirable to find a suitable low-cost material with a robust and environmentally friendly preparation method to fabricate supercapacitor with high energy and power densities.

Researchers are actively developing new and improved electrode materials to address the limitations of these metal oxides. The new materials focus on improving capacitance, cyclability, and cost-effectiveness.

Gallium oxide is a versatile material and expected to show high theoretical capacitance owing to the occurrence of multiple oxidation states that enable efficient energy storage [22]. In addition, Ga_2O_3 exhibits excellent chemical and thermal stability making it resistant to electrolytic degradation and corrosion resulting in longer cycle life and improved durability for supercapacitor applications. Gallium oxide can exist in several polymorphic forms: α, β, γ, δ, and ϵ [23,24]. β-Ga_2O_3 shows the highest stability comparing to the other four forms.

Ga_2O_3 boasts unique advantages, including a very simple preparation method as the element gallium melts at very low temperatures. This low temperature was the main reason for the preparation

of gallium oxide by the method described in this research. This aligns well with the growing demand for sustainable energy storage solutions. Additionally, Ga_2O_3 exists in multiple crystalline forms, offering the possibility to tailor its chemical properties for enhanced supercapacitor performance.

Although Ga_2O_3 research is limited in the context of supercapacitors, its low-cost and potentially expected high theoretical capacitance make it an attractive candidate for further investigation. Existing literature suggests limited inherent electrochemical activity in bulk Ga_2O_3. However, when employed in nanostructured forms, its properties may differ significantly. This research aims to explore the electrochemical properties of gallium oxide nanostructures and evaluate its potential as a promising material for high-performance supercapacitors. These are important instructions and explanations.

2. Materials and methods

Gallium oxide powder was prepared through a hydrothermal technique using a homemade stainless-steel cell [25]. 0.519 g of gallium (purity 99.999%) was added to 20 mL of hydrogen peroxide in the hydrothermal cell. The cell was moved to the programming furnace and kept at 250 ℃ for 24 h. The obtained white powder was then dried for 60 min at 60 ℃ and used without further treatment.

Rigaku Ultima IV X-Ray diffractometer was used to account for crystal structure investigation. The ESCALAB Xi + X-ray photoelectron spectrometer (XPS) was used to record the XPS spectra.

Porosity analysis was achieved using Nova 1200e (Quantachrome Ins). The physisorption isotherm was obtained through the use of N_2 gas at 77 K. The Brunauer, Emmett, and Teller (BET) model was applied to calculate the total surface area. The Dubinin-Astakhov (DA) method was used to quantify the pore radius and pore volume.

Before assembling the supercapacitor device, a few control experiments were performed. The first experiment aimed to test the suitability of a 316L stainless steel (SS) circular substrate (current collector) with a diameter of 0.9 cm for the current work. The blank 316L SS substrate was assembled into the working electrode as shown in Figure 1a. The working electrode was introduced into the electrochemical cell in a 3-electrode configuration. The electrolyte used was 1M KOH. Cyclic voltammetry (CV) was performed in the voltage range from 0 to 0.8 V at different scan rates of 50, 75 and 100 mV/s by the use of electrochemical workstation model PGSTAT302N (Metrohm AG). The second control experiment aimed to verify the redox activity of the prepared gallium oxide powder. For this purpose, a working electrode was fabricated as follows: 0.05 g of prepared Ga_2O_3 powder was added to 0.003 g of polyvinylidene fluoride (PVDF) and 1 mL of N-Methyl-2-pyrrolidone (NMP) was added to the powder mixture. The powder solution was stirred in a magnetic stirrer for 6 h. The gel powder slurry was then coated on the 316L stainless steel circular substrate. The substrate was transferred to a programming oven for 7 h at 100 ℃. After cooling, the circular substrate was assembled into the working electrode as shown in Figure 1b. Figure 1a,b show the actual working electrode before and after adding Ga_2O_3 powder. Using the assembled electrode, the CV experiment was performed in different electrolytes (1M KOH, 1M KCl and 1M H_2SO_4) at a scanning rate of 50 mV/s.

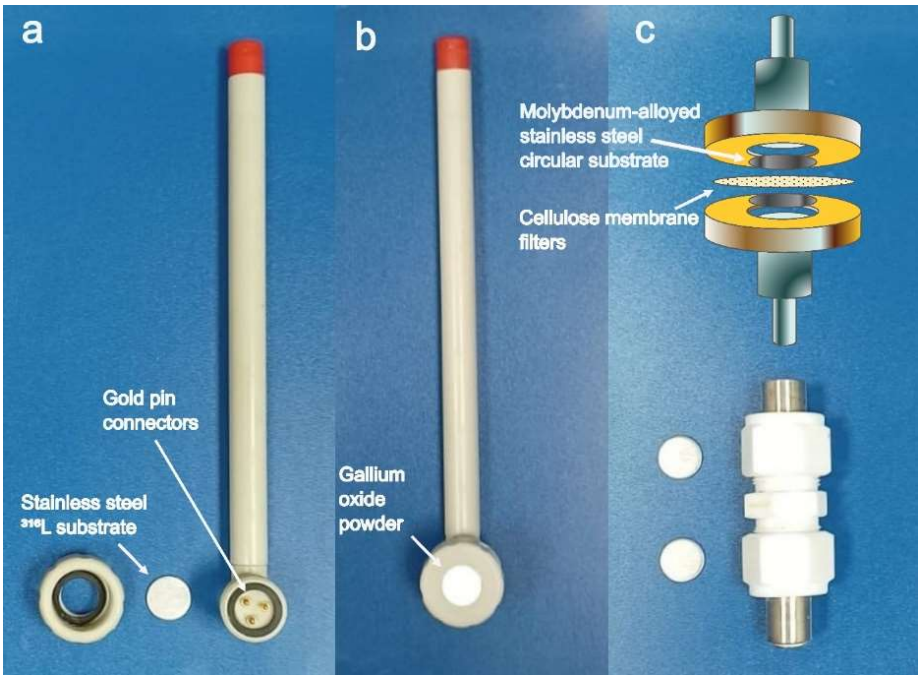

Figure 1. Actual images of: (a) working electrode components including 316L SS circular electrode, (b) working electrode with a loaded Ga_2O_3 powder, and (c) PFA Swagelok-type cell for supercapacitor measurements.

For device fabrication, Ga_2O_3 powder was mixed with 1M KOH to form a white paste. The obtained Ga_2O_3 paste was coated on two similar 316L SS substrates. The total mass on both substrates was estimated to be 10 mg. Cellulose membrane filters was used as a separator. The supercapacitor was assembled in PFA Swagelok-type cell for electrochemical measurements (Figure 1c). The filling electrolyte was 1M KOH. The electrochemical measurements were performed in a two-electrode cell. CV measurements were carried out at different scan rates, from 25 to 150 mV/s. Figure 2 shows schematic illustration of the work steps followed in this study.

In 3-electrode arrangement, a PDVF binder is used because the powder may fall into the electrolyte. The relatively large surface area is in direct contact with the electrolyte solution. However, in the two-electrode experiment, the powder is enclosed in a closed volume. Therefore, a binder is not necessary. In fact, we prefer to use the powder without any additional materials that might affect device performance. Although Ga_2O_3 powder itself is a dielectric material with no conductivity, its nanosize effect combined with the presence of excess Ga atoms can exhibit conductive behavior (as discussed later). In this way, other conductive materials, such as carbon, can be omitted. The excess Ga atoms can act as impurities or defects within the crystal structure. If Ga atoms occupy interstitial sites or substitute for oxygen atoms, they can donate extra electrons to the material, creating n-type conductivity. Introducing excess Ga can potentially induce phase transitions in Ga_2O_3, altering its electrical properties. However, controlling this process to achieve desired conductivity levels can be challenging. Othe possibility is the formation of Ga metal. Under specific conditions, excess Ga atoms might aggregate and form metallic Ga inclusions. These inclusions can create conductive pathways within the material, but this is often unintentional and can lead to inconsistent properties. Precisely controlling the location and concentration of excess Ga atoms is crucial for achieving predictable

conductivity. Achieving controlled and reliable conductivity through this method is complex and requires further experimentation and characterization.

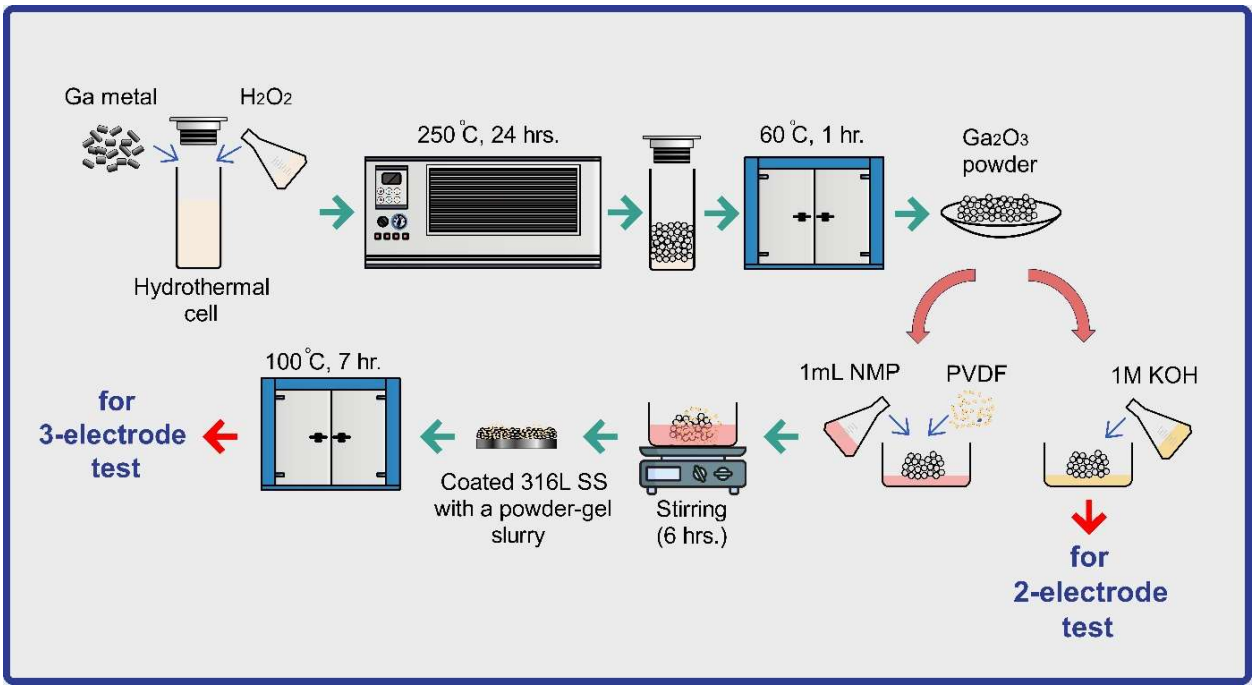

Figure 2. Schematic illustration of the work steps followed in this study.

The galvanostatic charge–discharge (GDC) measurements were achieved at different currents ranging from 2 to 15 A g^{-1} under a cutoff potential of 0.8 V vs. Ag/AgCl electrode. The calculations of specific capacitance C (F g^{-1}), energy density E (Wh kg^{-1}), and power density P (W kg^{-1}) are performed by the following relations (Eqs 1–3) [26]:

$$C = 2 \times \frac{I \times t}{\Delta V \times m} \tag{1}$$

$$E = \frac{1}{2} C \times \Delta V^2 \times \frac{1000}{3600} \tag{2}$$

$$P = \frac{E}{t} \times 3600 = \frac{I \times \Delta V}{m} \times 1000 \tag{3}$$

where I, t, ΔV and m are the discharge current (A), discharge time (s), the potential window (V), and the total mass of the active electrode material in both electrodes (g), respectively.

Electrochemical impedance measurements (EIS) were performed with the frequency range of 0.01 to 100 kHz at open-circuit potential with the amplitude of 10 mV. All electrochemical measurements were performed using 1M KOH as the electrolyte.

Some other important parameters are necessary to explore the full performance of the supercapacitor. These parameters include self-discharge current, coulomb efficiency (μ), and capacitance retention (CR). The coulombic efficiency, Eq 4 is defined as follows:

$$\mu(\%) = \frac{t_D}{t_C} \times 100 \tag{4}$$

where t_D and t_C are the discharge and charge times, respectively. The relation between μ, CR and number of cycles (n) is given by Eq 5 [27]:

$$\text{Capacity retention (CR) (\%)} = [\mu(\%)]^n \tag{5}$$

3. Results and discussion

Figure 3 shows the XRD pattern of the prepared gallium oxide powder. The pattern exhibited a polycrystalline nature. To examine the crystalline phases present, the XRD data were successfully indexed to two different PDF reference files (00-041-1103) and (01-074-1610). These files indicated the coexistence of different polymorphic forms, monoclinic β-Ga_2O_3 and rhombohedral α-Ga_2O_3, respectively. While the monoclinic structure is stable and dominant, the other structure is produced as a result of high pressure inside the hydrothermal cell. The formation of rhombohedral (β-Ga_2O_3) is attributed to the phase transition of gallium hydroxide (GaOH) to gallium oxide under high pressure [28].

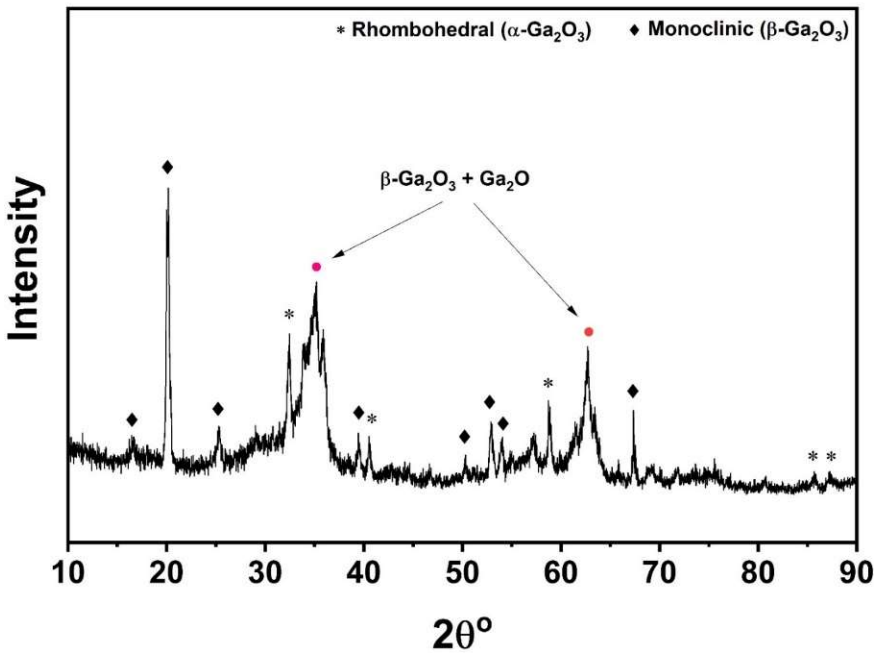

Figure 3. XRD pattern of gallium oxide powder produced by a hydrothermal method.

The scanning electron microscopy (SEM) images revealed a material with a fascinatingly diverse morphology, composed of various nanostructures with different sizes and shapes, Figure 4a. Elongated rods with hexagonal cross-sections and relatively large diameters are observed (Figure 4a,b). Interconnecting rods are also observed (Figure 4c–f). The presence of these rods suggests a network-like structure, which could be beneficial for mechanical stability and potentially create pathways for electrical conduction. The interconnected rods and possibly some nanoparticles could form a conductive network, making the material useful as electrodes. Transmission electron microscopy (TEM) images

of gallium oxide powder are shown in (Figure 4g–i). It is clear that several structure phases are present, such as nanoparticles and nanosheets as shown in Figure 4g,h. Spherical nanoparticles are clearly shown in Figure 4i. While SEM revealed a diverse morphology with rods (various sizes) and large-area nanosheets. Its resolution is lower compared to TEM, making it difficult to distinguish very small nanoparticles or ultra-thin features. On other hand TEM images confirmed the presence of spherical nanoparticles and nanosheets. The presence of nanoparticles and nanosheets also suggests a high surface area, allows for more interaction with surrounding electrolytes. The combination of these nanostructures suggests a potentially multifunctional material.

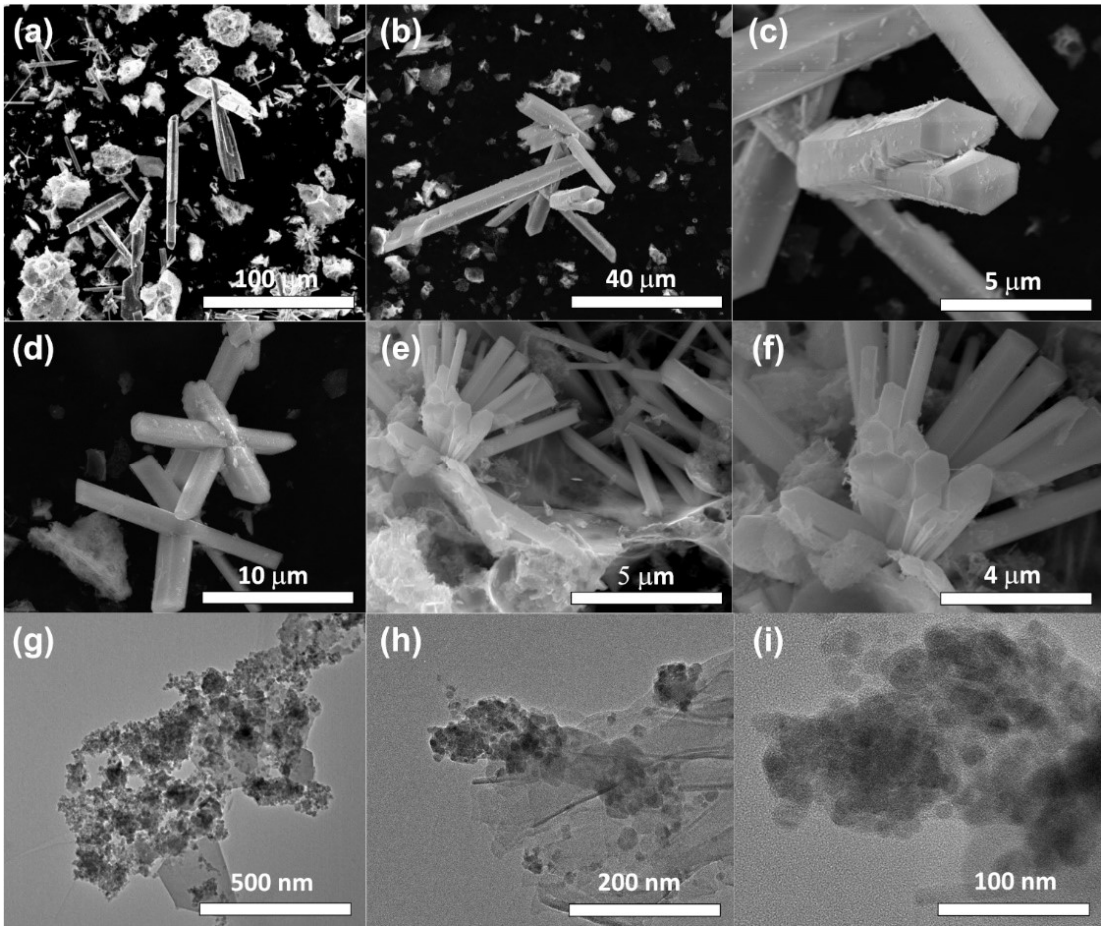

Figure 4. SEM images of the gallium oxide powder: (a) nanostructures with different sizes and shapes, (b) large rods, (c) rods with hexagonal cross-sections, (d) interconnecting rods, and (e,f) interconnecting rods with different magnifications. TEM images of the gallium oxide powder: (g) mixed nanostructure phases, such as nanoparticles and large area nanosheets (with different shapes), (h) small rods, and (i) spherical nanoparticles.

Figure 5a shows the XPS survey spectrum of Ga_2O_3 powder. All characteristic peaks for Ga_2O_3 are clearly visible in the spectrum [29,30]. High-resolution spectra of the O 1s and Ga 2p doublet core levels are presented in Figure 5b,c, respectively. XPS analysis of Ga_2O_3 typically does not show a significant chemical shift in the Ga binding energy, see Table 1.

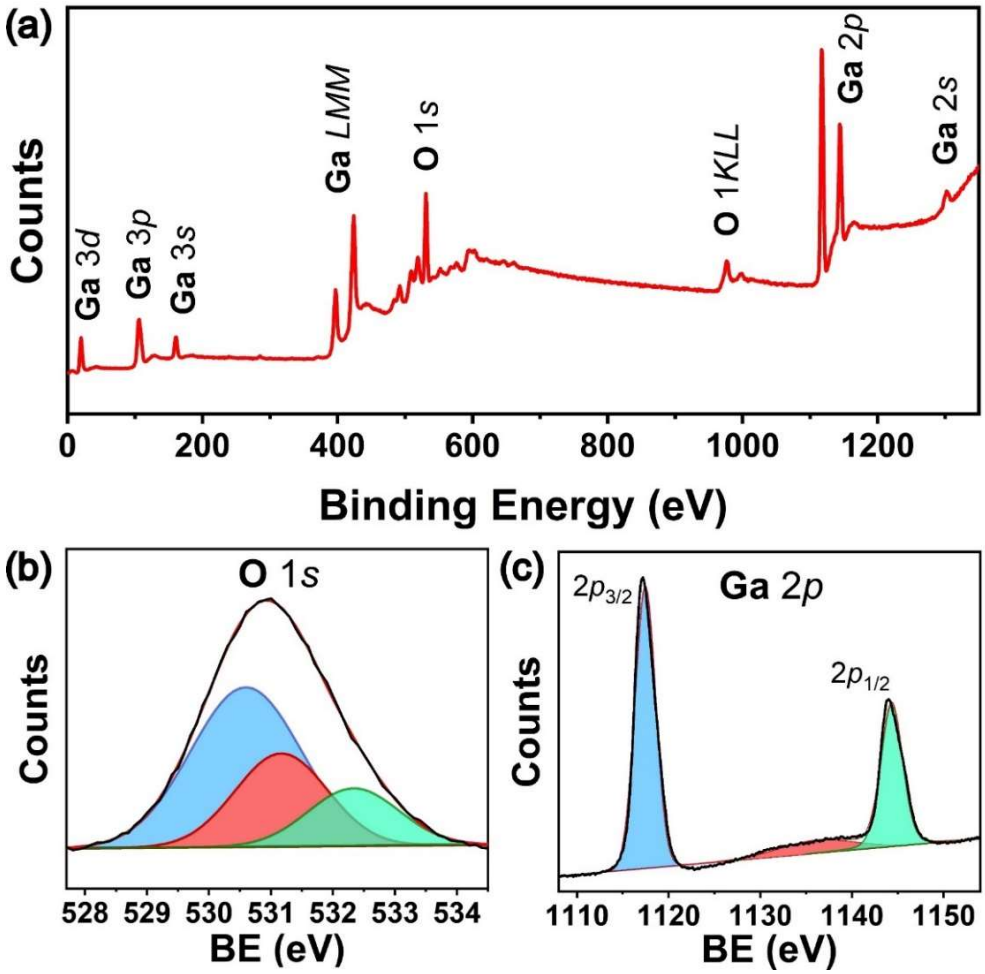

Figure 5. XPS spectra of Ga_2O_3 powder: (a) survey spectrum, (b) high-resolution O 1s peak profile, and (c) high-resolution Ga 2p peak profile.

Table 1. XPS core level peaks for Ga_2O_3 powder.

Ga 3*d*	Ga 3*p*	Ga 3*s*	Ga $2p_{3/2}$	Ga $2p_{1/2}$	Ga 2*s*	O 1*s*	Ref
20.5	105.5	159.0	1116.0–1118.0	1144.0	1301.0	531.0	[29–32]
20.0	105.7	160.4	1117.6	1144.3	1301.2	530.9	This work

The Ga 2p doublet peak is the most prominent feature in Ga_2O_3 XPS spectra [32]. In Ga_2O_3, the expected binding energy for Ga $2p_{3/2}$ is around 1117 eV, corresponding to the Ga^{3+} oxidation state. A significant deviation from this value could indicate the presence of Ga in other oxidation states or different chemical environments. Here, the obtained binding energy of the Ga $2p_{3/2}$ peak is typically around 1117.6 eV, indicating the Ga^{3+} oxidation state. The deconvolution of the Ga $2p_{1/2}$ peak into two peaks suggests the presence of two distinct chemical environments for gallium within the material. Surface gallium atoms can have slightly different chemical environments and binding energies compared to those in the bulk. Thus, these two peaks likely correspond to gallium existing in different oxidation states. The higher binding energy peak (1144.3 eV) is generally attributed to Ga^{3+}, the typical oxidation state in Ga_2O_3. The lower binding energy peak (1136.5 eV) might be due to reduced gallium

species with a lower oxidation state, such as Ga^{1+}, which is the characteristic oxidation state of gallium suboxide (Ga_2O). Alternatively, the presence of the two peaks could also indicate non-stoichiometry in the Ga_2O_3. This means that the material deviates from its ideal Ga:O atomic ratio (40%:60%). This can lead to the formation of defects like gallium vacancies or oxygen vacancies, contributing to the lower binding energy peak. The obtained Ga:O atomic ratio from XPS analysis (47.23%:52.77%) confirms this possibility. The formation of gallium suboxide Ga_2O is due to the presence of much Ga atoms during the preparation process. Gallium suboxide (Ga_2O) can be produced by reacting Ga_2O_3 with heated Ga in a hydrothermal cell under high pressure. The reaction can be represented by the Eq 6 as follows:

$$Ga_2O_3 + 4\ Ga \rightarrow 3\ Ga_2O \tag{6}$$

XRD analysis of Ga_2O_3 occasionally shows broad peaks, indicating a disordered or poorly defined crystal structure. This is clear in Figure 3 where, the peaks at 35.14° and 62.68° are broad and disordered. Therefore, unlike pure Ga_2O_3 phase with its well-defined crystal structure, Ga_2O suboxide exhibits a more complex and less characterized non-crystalline structural arrangement. A previous study showed that significant oxygen deficiency in gallium oxide can lead to the formation of a composite material combining crystalline β-Ga_2O_3 and non-crystalline gallium suboxide Ga_2O [33].

In Ga_2O_3, the expected binding energy for O 1s is around 531 eV, characteristic of the Ga–O bond. Here, the O 1s reveals broader peak due to multiple bonding environments in Ga_2O_3. The deconvolution of O 1s revealed three distinct peaks. The main peak at the lowest binding energy (around 530.8 eV) corresponds to the majority of oxygen atoms bound to gallium (Ga–O) within the Ga_2O_3 lattice [29,30]. The absence of a significant shift from the expected value of 531 eV generally indicates that the dominant chemical environment for oxygen in the sample is Ga_2O_3. The second peak at a slightly higher binding energy (around 531.2 eV) with lower intensity can be attributed to the presence of oxygen vacancies within the Ga_2O_3 lattice [34]. Oxygen vacancies can occur during the growth process of the powder. This peak can also be associated with hydroxyl groups (OH) adsorbed on the Ga_2O_3 surface due to exposure to water vapor in the environment [35]. The broadest peak at the highest binding energy (around 532.4 eV) might be due to oxygen atoms in adsorbed species like water molecules on the Ga_2O_3 surface. This peak is rarely reported and might, in some cases, be attributed to a very small fraction of gallium in higher oxidation states (Ga_2O_5) on the surface [36]. Moreover, there is a minor shift (0.2 eV) in the Ga 3p binding energy is observed. This can be attributed to factors like differences in the Ga environment at the surface compared to the bulk. No other distinct peaks are observed indicating the high purity of the prepared powder. The peak observed at around 400 eV likely corresponds to the GaLMM Auger electron emission.

Figure 6a shows the physisorption isotherm of gallium oxide powder. The shown isotherm exhibited IV(a)-type indicating that the size of the present pores is in the range of 1–100 nm. Multipoint BET method was utilized to deduce the total surface area of the powder, Figure 6b. The calculated value was 50.564 $m^2\ g^{-1}$. Figure 6c shows the surface area histogram. The pore diameter distribution was obtained by using Dubinin–Astakhov (DA) method. Figure 6d shows the pore-diameter distribution curve. The curve shows a peak located at 2.6 nm and the calculated nanopores volume was found to be around 0.07 $cm^3\ g^{-1}$.

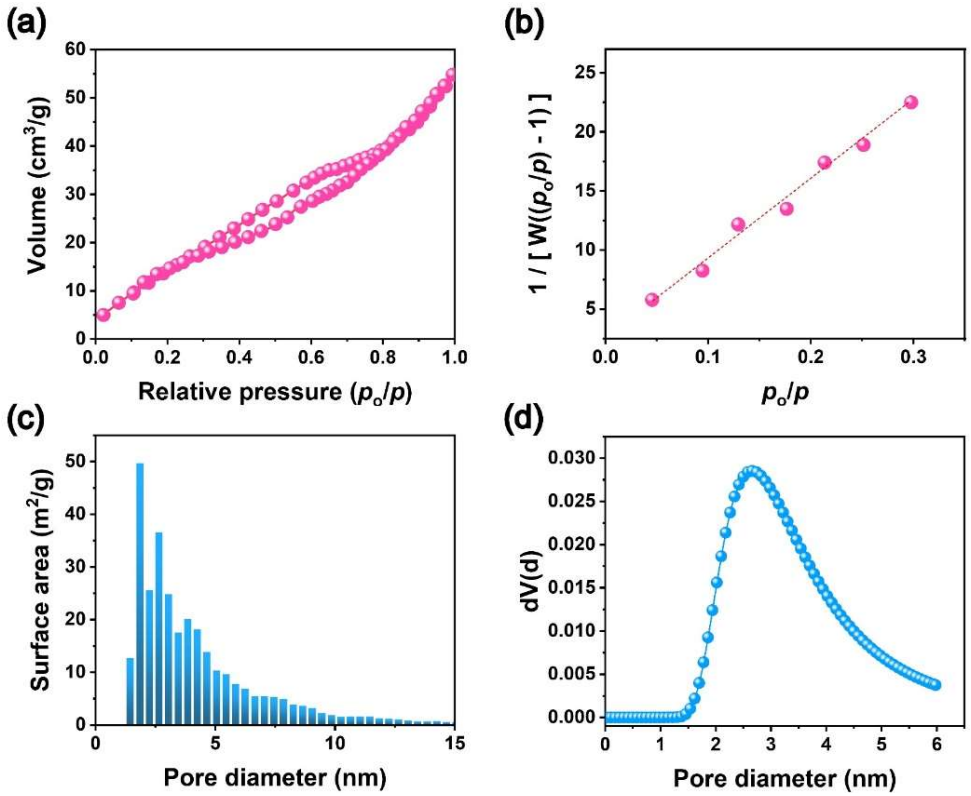

Figure 6. Porosity analysis of gallium oxide powder. (a) Physisorption isotherm (type IV[a]), (b) BET plot for surface area calculation, (c) surface area distributions, and (d) pore diameter distribution.

Figure 7a shows the CV curves of the bare 316L SS substrate. The absence of any redox peaks indicates that the substrate exhibits no redox activity. Repeated measurements did not reveal any visible signs of corrosion. These results suggest the suitability of the 316L SS substrate as a current collector for fabricating and characterizing Ga_2O_3-based supercapacitors. In the alkaline electrolyte the CV curve exhibits sharp and well-defined redox peaks (Figure 7b). These peaks correspond to reversible redox reactions of the metal oxide. This behaviour confirms that Ga_2O_3 exhibits pseudocapacitive characteristics, suggesting a different energy storage mechanism compared to ideal supercapacitors. Ideal supercapacitors exhibit rectangular CV curves and store energy through electrostatic double-layer capacitance (EDLC). EDLC involves the separation of charges at the electrode-electrolyte interface without electron transfer into the electrode bulk. This mechanism provides high power density, fast charge/discharge rates, and long cycle life. Materials with redox peaks store energy through a combination of EDLC and Faradaic processes. Faradaic processes involve electron transfer between the electrode material and the electrolyte ions. This combination can achieve higher energy density compared to pure EDLC materials. Therefore, Ga_2O_3, which shows redox peaks in its CV curve, is a promising candidate for supercapacitors due to its potential for higher energy density. The CV curve measured in neutral electrolytes shows no redox peaks compared to alkaline electrolyte. In acidic electrolytes CV curve is complex with multiple broad peaks due to various possible redox reactions and side reactions. The acidity can also lead to dissolution of the metal oxide, affecting the overall shape of the curve. Accordingly, a 1 M KOH solution was used for device characterization.

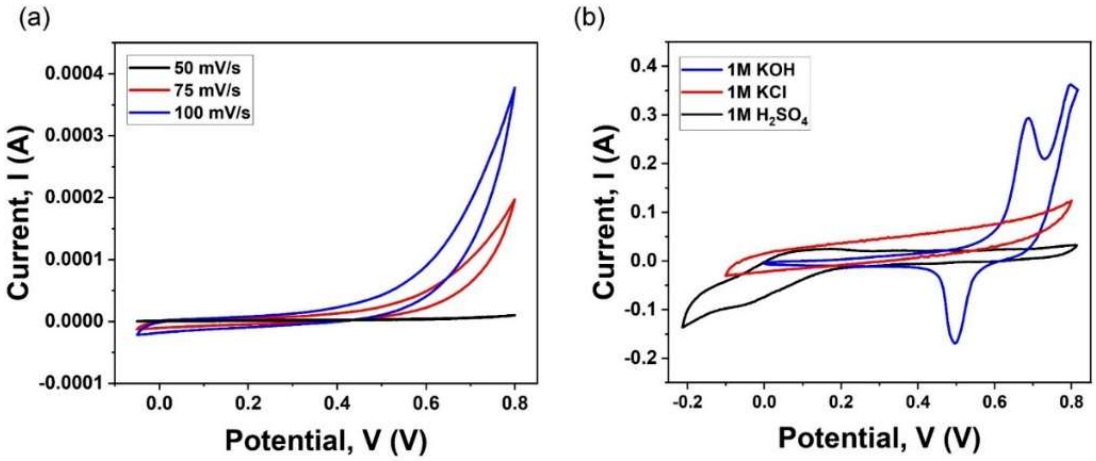

Figure 7. CV curves of: (a) bare 316L SS substrate at different scanning rates and (b) Ga_2O_3 electrode in different electrolytes.

Figure 8a shows the galvanostatic charge/discharge (GCD) curves of the fabricated supercapacitor at different constant currents. The GCD curves all maintain a relatively good triangular shape. The fabricated supercapacitor provides a maximum capacitance of 1176 F g^{-1}, an energy density of 104.5 Wh kg^{-1} and an equivalent high-power density of 1.6 kW kg^{-1} at a specific current of 2 A g^{-1}. The maximum specific capacitance obtained at 2 A g^{-1} has higher value than most of the reported materials [37–45]. As the current density increased, the specific capacitance decreased significantly. This can be attributed to the reduction of electrolyte ions due to their absorption by the double layer formed at the electrode/electrolyte interface.

Figure 8b illustrates the behavior of specific capacitance as a function of the number of charge-discharge cycles (capacitance retention) of a Ga_2O_3-based supercapacitor at a charging-discharging current of 10 A g^{-1}. The coulombic efficiency as well as energy efficiency are also presented. It is concluded that, the capacitance endured at nearly 92% after 5000 cycles which disclosed no weighty capacity loss, indicating outstanding cycle stability. This indicates that the Ga_2O_3-based supercapacitor possesses superior electrochemical reversibility and good device performance. Moreover, a high coulombic efficiency of nearly 100% signifies that almost all the charge stored during the charging cycle is delivered back during the discharging cycle. While achieving an energy efficiency of 93% confirms its exceptional ability to store and deliver charge with minimal losses, demonstrating long-term reliability and high energy efficiency.

To study self-discharging, the supercapacitor is fully charged with a certain voltage and then the steady decrease in voltage is monitored as a function of time. The observed self-discharge behavior cannot be solely explained by the ohmic leakage mechanism concept because the self-discharge curves in Figure 8c deviate from a purely exponential decay. Since self-discharge in a supercapacitor is unavoidable, various strategies have been explored to reduce it, including fine-tuning the electrode materials, adding additives into the electrolyte, and utilizing ion-exchange membranes as separators.

Figure 8d shows CV curves of the fabricated supercapacitor at different scan rates. All CV curves exhibit rectangular shapes, with their areas increasing as the scan rate increases. This suggests that the Ga_2O_3 powder has excellent capacitive behavior. The absence of pseudocapacitance behavior suggests that the energy storage mechanism in the supercapacitor is primarily based on the formation of an

electrical double layer capacitance rather than redox reactions. This non-faradaic process involves the accumulation of charges at the electrode-electrolyte interface. The specific capacitance can be also obtained from CV data, using Eq 7 as follows:

$$C = \frac{1}{m\theta(V_b - V_a)} \int_{V_1}^{V_2} I \, dV \tag{7}$$

where, m is the total mass of active materials loaded on two electrodes, θ (V s^{-1}) is the scan rate, and V_1 and V_2 are potential boundaries of the CV curves. The factor $\int$ I dV is the integrated area of CV curve. The accuracy of the obtained capacitance depends on the shape of CV curves. A rectangular shape with no peaks is the typical shape for a supercapacitor. In the case of non-rectangular or peak-shaped the calculation for capacitance should be avoided. Although Figure 8d shows CV curves with no peaks but still exhibits flattened and not exactly rectangular shape. Just for completeness, the maximum obtained capacitance from CV curves is found to be 561 F g^{-1} at 25 mV/s. Figure 8e shows the obtained capacitances vs scan rates.

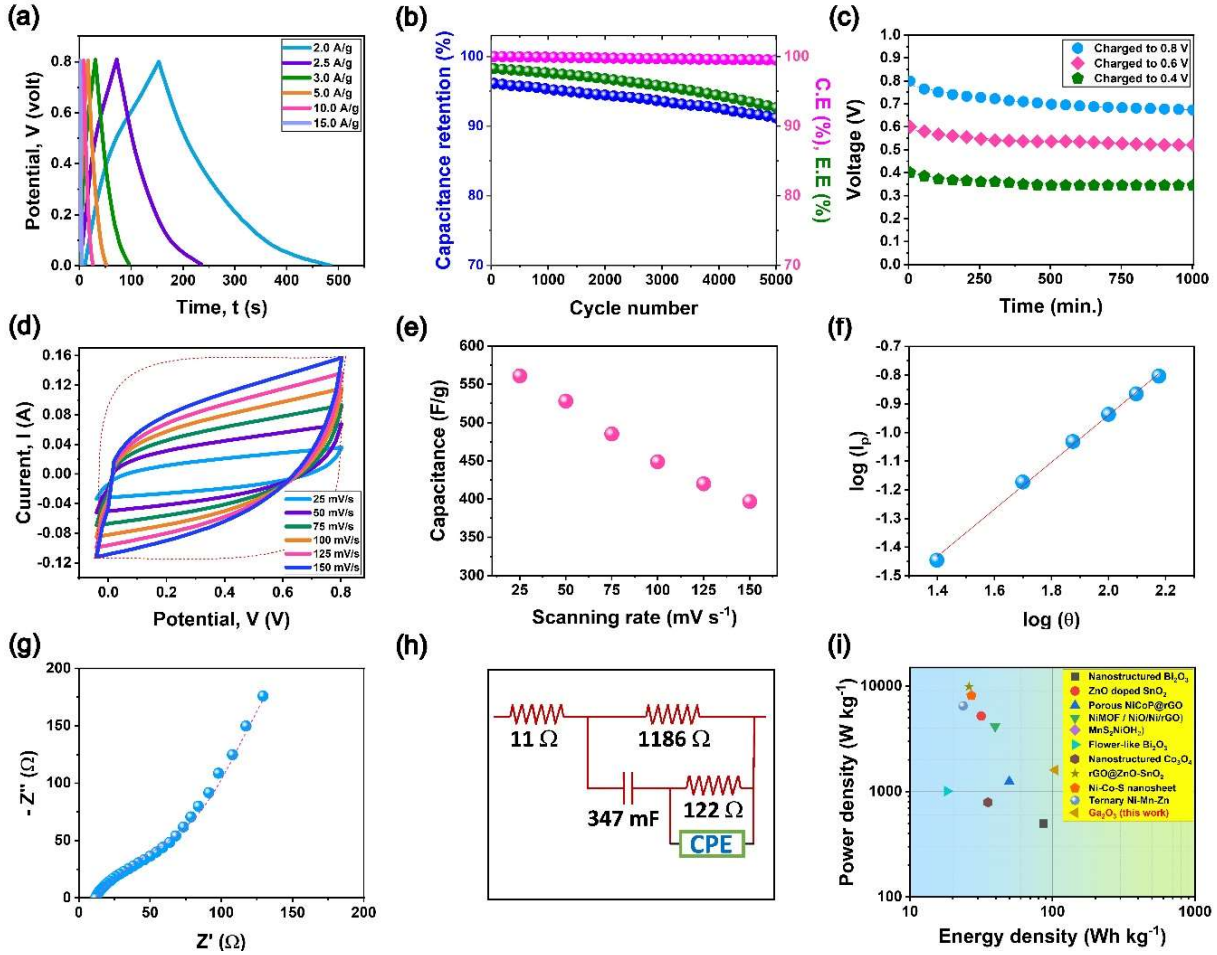

Figure 8. (a) Charge-discharge curves, (b) capacitance retention and coulombic efficiency, (c) self-discharge, (d) CV curves, (e) capacitances vs scanning rate, (f) a graph of log i vs log θ, (g) Nyquist plot, (h) the corresponding equivalent circuit, and (i) Ragone plot.

To explore the types of storage mechanism involved, Eq 8 will be employed for the analysis of CV data [46]:

$$i = a\theta^b \tag{8}$$

where *a* and *b* are constants and *i* represents the anodic (or cathodic) peak current (A). Accordingly, a graph of log i vs log θ is established, see Figure 8f. The slope of the obtained straight line is the value of b in Eq 8. This value was found to be 0.8 which is neither 0.5 nor 1, indicating that the storage mechanism is a surface charge coupled with solid-state (bulk) diffusion-limited process This conclusion is consistent with EIS study where semicircle and an incline straight line are obtained in a Nyquist plot, Figure 8g. The figure exhibits a non-ideal semicircle shape and a straight line inclined with the x-axis by about 50^o indicating the formation of a non-ideal capacitance at the electrode/electrolyte interface. The equivalent circuit of the supercapacitor is also shown in the Figure 8h. This Nyquist plot displays a distorted, flattened and depressed semicircle instead of an ideal semicircle in the high frequency domain and an inclined vertical line in the low-frequency domain indicating the capacitive act of the Ga_2O_3. The most common circuit element for modeling this non-ideal behavior is the constant phase element (CPE). CPE is usually observed when solid electrodes come into contact with an electrolyte, resulting in the formation of a double-layer capacitor [29]. The mathematical definition of CPE impedance, Eq 9, is frequently used to describe this phenomenon [47]:

$$Z_{CPE} = \frac{1}{Q(j\omega)^n} \tag{9}$$

where *n* is a number between 0 and 1. If $n = 1$, it is pure capacitance; if $n = 0$, it is pure resistance. If CPE is used alone, its Nyquist plot is a straight line with a certain angle relative to the real axis. The phase angle of the CPE element is independent of the frequency and has a value of $(-90 \times n)^o$. The Q parameter has units of F s$(n^{-1})m^{-2}$, which have no real physical meaning. When a parallel combination of resistance R (charge transfer resistance) and CPE is proposed, it is possible to determine the actual double layer capacitance behind the CPE by Eq 10 [48]:

$$C_{dl} = \frac{(R \times Q)^{\frac{1}{n}}}{R} \tag{10}$$

The obtained value for double layer capacitance is 0.9 μF. The obtained double layer resistance is 122 Ω which is much higher than the electrolyte resistance (11 Ω) which reduces the access of more electrolyte ions to the electrodes.

The fabricated supercapacitor demonstrates high energy density, 104.5 W kg^{-1}, (battery-like) coupled with high power density, 1.6 kWh g^{-1} (supercapacitor-like) behaviors, as shown in the Ragone plot (Figure 8i). The obtained high values of energy and power densities can be attributed to the coexistence of multiple phases of the Ga_2O_3. The non-stochiometric composition creates more rooms for charge storage and enhances the capacitive properties of the fabricated supercapacitor. The multiple phases of the Ga_2O_3 result in a material with a unique crystal structure that allows for the coexistence of different crystal orientations within a single crystal. This 'multidirectional' arrangement configuration holds substantial significance for the electronic properties and, consequently, its energy storage capabilities. Multidirectional Ga_2O_3 often exhibits a reduced number of grain boundaries, which are regions where charge carriers may experience scattering, consequently diminishing their mobility. This variety of arrangement leads to enhanced charge transport and increased conductivity.

The coexistence of different crystal orientations may also create pathways for charge carriers to move efficiently in various directions, thereby enhancing mobility. Additionally, the diversity of crystal orientations and surface terminations can generate an array of active sites for electrochemical reactions. Such assortment can significantly improve the overall electrochemical performance of the material. The interplay between different crystal orientations and surface terminations may yield synergistic effects, that enhancing the overall performance of the material. These factors collectively contribute to the high energy and power density that observed in multiple phases Ga_2O_3.

Table 2. Supercapacitors comparison on the basis of energy and power densities.

Supercapacitors	Specific capacitance ($F\ g^{-1}$)	Energy density ($Wh\ Kg^{-1}$)	Power density ($kW\ kg^{-1}$)	Ref
RGO@ZnO-SnO_2	-	26.00	9.870	[49]
ZnO doped SnO_2	392	31.60	5.200	[38]
Nanostructured Bi_2O_3	-	86.40	0.498	[39]
Porous NiCoP@rGO	146	49.80	1.246	[40]
Ternary Ni-Mn-Zn	-	23.64	6.499	[50]
Ni-MOF & NiO/Ni/r-GO	-	39.59	4.136	[41]
MnS@$Ni(OH)_2$l	169	60.00	0.800	[42]
Ni-Co-S nanosheet	-	27.00	8.115	[43]
Flower-like Bi_2O_3	36	18.24	1.008	[44]
Nanostructure Co_3O_4	-	35.30	0.789	[45]
Nanostructure Ga_2O_3	1176	104.50	1.600	This work

4. Conclusions

In this study, gallium oxide powder was successfully prepared by a simple hydrothermal method. XRD results indicated the coexistence of three different phases, monoclinic (β-Ga_2O_3), rhombohedral (α-Ga_2O_3) and gallium suboxide Ga_2O. XPS analysis confirmed Ga^{3+} as the dominant oxidation state of gallium within the material. However, the presence of a lower oxidation state, Ga^{1+}, was also detected. The porosity analysis was carried out and the obtained values of the total surface area, pore diameter, and pore volume of the gallium oxide powder were 50 $m^2\ g^{-1}$, 2.6 nm, and 0.07 $cm^3\ g^{-1}$, respectively. The fabricated supercapacitor delivered a maximum capacitance of 1176 $F\ g^{-1}$, an energy density of 104.5 $Wh\ kg^{-1}$ and an equivalent high-power density of 1.6 $kW\ kg^{-1}$ at a specific current of 2 $A\ g^{-1}$. This supercapacitor demonstrates remarkable characteristics, achieving both high energy density and high-power density, in addition to the ecofriendly and easy fabrication method. These exceptional values can be attributed to the presence of multiple Ga_2O_3 phases in the electrode material. The non-stochiometric composition creates more rooms for charge storage and enhances the capacitive properties of the fabricated device. Overall, Ga_2O_3 holds a great potential for supercapacitors due to its exceptional theoretical capacitance, fast kinetics, remarkable stability, and environmental friendliness. By addressing surface area and processing challenges, Ga_2O_3 could pave the way for the next generation of high-performance supercapacitors, enabling efficient and sustainable energy storage solutions for a wide range of applications.

Use of AI tools declaration

The authors declare they have not used Artificial Intelligence (AI) tools in the creation of this article.

Author contributions

Conceptualization: A.A. and E.S.; data curation: J.A., E.S; investigation: J.A. and E.S.; methodology: J.A., A.A. and E.S.; resources: A.A. and E.S.; supervision: A.A. and E.S.; writing—original draft preparation: J.A.; writing—review and editing: J.A., A.A. and E.S. All authors have read and agreed to the published version of the manuscript.

Conflict of interest

The authors declare no conflict of interest.

References

1. Yang YB, Zhu SM, Xu HF (2022) Study on capacitance properties of redox ion doped Zn-based electrode materials. *Defect Diffus Forum* 421: 143–148. https://doi.org/10.4028/p-u2pe4h
2. Jayakumar S, Santhosh PC, Mohideen MM, et al. (2024) A comprehensive review of metal oxides (RuO_2, Co_3O_4, MnO_2 and NiO) for supercapacitor applications and global market trends. *J Alloys Compd* 976: 173170. https://doi.org/10.1016/j.jallcom.2023.173170
3. Majumdar D, Maiyalagan T, Jiang Z (2019) Recent progress in ruthenium oxide-based composites for supercapacitor applications. *ChemElectroChem* 6: 4343–4372. https://doi.org/10.1002/celc.201900668
4. Sugimoto W (2014) Ruthenium oxides as supercapacitor electrodes, In: Kreysa G, Ota Ki, Savinell RF, *Encyclopedia of Applied Electrochemistry*, New York: Springer, 1813–1821. https://doi.org/10.1007/978-1-4419-6996-5_511
5. Nisha B, Vidyalakshmi Y, Abdul Razack S (2020) Enhanced formation of ruthenium oxide nanoparticles through green synthesis for highly efficient supercapacitor applications. *Adv Powder Technol* 31: 1001–1006. http://dx.doi.org/10.1016/j.apt.2019.12.026
6. Guo Y, Zhu Z, Chen Y, et al. (2020) High-performance supercapacitors of ruthenium-based nanohybrid compounds. *J Alloys Compd* 842: 155798. https://doi.org/10.1016/j.jallcom.2020.155798
7. Kim IH, Kim KB (2001) Ruthenium oxide thin film electrodes for supercapacitors. *Electrochem Solid-State Lett* 4: A62. https://iopscience.iop.org/article/10.1149/1.1359956
8. Zhang M, Dai X, Zhang C, et al. (2020) High specific capacitance of the electrodeposited MnO_2 on porous foam Nickel soaked in alcohol and its dependence on precursor concentration. *Materials* 13: 181. https://doi.org/10.3390/ma13010181
9. Brousse T, Bélanger D, Long JW (2015) To be or not to be pseudocapacitive? *J Electrochem Soc* 162: A5185. http://dx.doi.org/10.1149/2.0201505jes

10. Lang X, Hirata A, Fujita T, et al. (2011) Nanoporous metal/oxide hybrid electrodes for electrochemical supercapacitors. *Nat Nanotechnol* 6: 232–236. https://doi.org/10.1038/nnano.2011.13
11. Ryu I, Kim G, Yoon H, et al. (2016) Hierarchically nanostructured MnO_2 electrodes for pseudocapacitor application. *RSC Adv* 6: 102814–102820. https://doi.org/10.1039/C6RA22841K
12. Liu Y, Liu S, Wang X, et al. (2023) One-step synthesis of self-standing porous Co-doped NiO electrodes for high-performance supercapacitors. *J Alloys Compd* 934: 167821. https://doi.org/10.1016/j.jallcom.2022.167821
13. Manibalan G, Govindaraj Y, Yesuraj J, et al. (2021) Facile synthesis of NiO@$Ni(OH)_2$-α-MoO_3 nanocomposite for enhanced solid-state symmetric supercapacitor application. *J Colloid Interface Sci* 585: 505–518. https://doi.org/10.1016/j.jcis.2020.10.032
14. Veeresh S, Ganesha H, Nagaraju YS, et al. (2023) Activated carbon incorporated graphene oxide with SnO_2 and TiO_2-Zn nanocomposite for supercapacitor application. *J Alloys Compd* 952: 169907. https://doi.org/10.1016/j.jallcom.2023.169907
15. Asen P, Haghighi M, Shahrokhian S, et al. (2019) One step synthesis of SnS_2-SnO_2 nano-heterostructured as an electrode material for supercapacitor applications. *J Alloys Compd* 782: 38–50. https://doi.org/10.1016/j.jallcom.2018.12.176
16. Huang X, Zhang W, Tan Y, et al. (2016) Facile synthesis of rod-like Bi_2O_3 nanoparticles as an electrode material for pseudocapacitors. *Ceram Int* 42: 2099–2105. https://doi.org/10.1016/j.ceramint.2015.09.157
17. Wu YL, Guo W, Lian XJ, et al. (2019) Self-assembled three-dimensional hierarchical $CoMoO_4$ nanosheets on $NiCo_2O_4$ for high-performance supercapacitor. *J Alloys Compd* 793: 418–424. https://doi.org/10.1016/j.jallcom.2019.04.189
18. Nandagopal T, Balaji G, Vadivel S (2023) Enhanced electrochemical performance of $CoMoO_4$ nanorods/reduced graphene oxide (rGO) as asymmetric supercapacitor devices. *J Energy Storage* 68: 107710. https://doi.org/10.1016/j.est.2023.107710
19. Gao Y, Tao J, Li J, et al. (2022) Construction of $CoMoO_4$ nanorods wrapped by Ni–Co–S nanosheets for high-performance supercapacitor. *J Alloys Compd* 925: 166705. https://doi.org/10.1016/j.jallcom.2022.166705
20. Jiang S, Pang M, Pang M, et al. (2023) 3D emerging nanosheets comprising hierarchical $CoMoO_4$/MnO_2 composites for flexible all-solid-state asymmetric supercapacitors. *Colloids Surf A* 656: 130536. https://doi.org/10.1016/j.colsurfa.2022.130536
21. Nasser R, Wang XL, Tiantian J, et al. (2022) Hydrothermal design of $CoMoO_4$@$CoWO_4$ core-shell heterostructure for flexible all-solid-state asymmetric supercapacitors. *J Energy Storage* 51: 104349. http://dx.doi.org/10.1016/j.est.2022.104349
22. Nashim A, Mohanty R, Ray PK, et al. (2023) Gallium-based nascent electrode materials towards promising supercapacitor applications: A review. *RSC Adv* 13: 24536–24553. https://doi.org/10.1039/D3RA04537D
23. Roy R, Hill VG, Osborn EF (1952) Polymorphism of Ga_2O_3 and the system Ga_2O_3–H_2O. *J Am Chem Soc* 74: 719–722. https://doi.org/10.1021/ja01123a039
24. Lyons JL (2019) Electronic properties of Ga_2O_3 polymorphs. *ECS J Solid State Sci Technol* 8: Q3226. http://dx.doi.org/10.1149/2.0331907jss

25. El-Sayed EI, Al-Ghamdi AA, Al-Heniti S, et al. (2011) Synthesis of ultrafine β-Ga_2O_3 nanopowder via hydrothermal approach: A strong UV "excimer-like" emission. *Mater Lett* 65: 317–321. https://doi.org/10.1016/j.matlet.2010.10.007
26. Yu J, Fu N, Zhao J, et al. (2019) High specific capacitance electrode material for supercapacitors based on resin-derived nitrogen-doped porous carbons. *ACS Omega* 4: 15904–15911. https://doi.org/10.1021/acsomega.9b01916
27. Tornheim A, O'Hanlon DC (2020) What do coulombic efficiency and capacity retention truly measure? A deep dive into cyclable lithium inventory, limitation type, and redox side reactions. *J Electrochem Soc* 167: 110520. http://dx.doi.org/10.1149/1945-7111/ab9ee8
28. Pearton SJ, Yang J, Cary PHIV, et al. (2018) A review of Ga2O3 materials, processing, and devices. *Appl Phys Rev* 5: 011301. http://dx.doi.org/10.1063/1.5006941
29. Briggs D (1981) Handbook of X-ray photoelectron spectroscopy, In: Wanger CD, Riggs WM, Davis LE, et al. *Physical Electronics Division*, Minnesota: John Wiley & Sons. https://doi.org/10.1002/sia.740030412
30. Moulder JF, Stickle WF, Sobol WM, et al. (1992) Handbook of X-ray photoelectron spectroscopy.
31. Swallow JEN, Vorwerk C, Mazzolini P, et al. (2020) Influence of polymorphism on the electronic structure of Ga_2O_3. *Chem Mater* 32: 8460–8470. http://dx.doi.org/10.1021/acs.chemmater.0c02465
32. Makeswaran N, Battu AK, Swadipta R, et al. (2019) Spectroscopic characterization of the electronic structure, chemical bonding, and band gap in thermally annealed polycrystalline Ga_2O_3 thin films. *ECS J Solid State Sci Technol* 8: Q3249. http://dx.doi.org/10.1149/2.0461907jss
33. Vogt P, Bierwagen O (2016) Reaction kinetics and growth window for plasma-assisted molecular beam epitaxy of Ga_2O_3: Incorporation of Ga vs. Ga_2O desorption. *Appl Phys Lett* 108: 072101. http://dx.doi.org/10.1063/1.4942002
34. Azarov A, Park JH, Jeon DW, et al. (2023) High mobility of intrinsic defects in α-Ga_2O_3. *Appl Phys Lett* 122: 182104. http://dx.doi.org/10.1063/5.0149870
35. Pratiyush AS, Krishnamoorthy S, Muralidharan R, et al. (2019) 16—Advances in Ga_2O_3 solar-blind UV photodetectors, In: Pearton S, Ren F, Mastro M, *Gallium Oxide*, Amsterdam: Elsevier, 369–399. https://doi.org/10.1016/C2017-0-01768-8
36. Lee YJ, Schweitz MA, Oh JM, et al. (2020) Influence of annealing atmosphere on the characteristics of Ga_2O_3/4H-SiC n-n heterojunction diodes. *Materials* 13: 434. https://doi.org/10.3390/ma13020434
37. Zhang P, Li Y, Wang M, et al. (2023) Self-doped (N/O/S) nanoarchitectonics of hierarchically porous carbon from palm flower for high-performance supercapacitors. *Diam Relat Mater* 136: 109976. https://doi.org/10.1016/j.diamond.2023.109976
38. Molahalli V, Bhat VS, Shetty A, et al. (2023) ZnO doped SnO_2 nano flower decorated on graphene oxide/polypyrrole nanotubes for symmetric supercapacitor applications. *J Energy Storage* 69: 107953. https://doi.org/10.1016/j.est.2023.107953
39. Fei F, Zhou H, Lin J, et al. (2023) Facile synthesis of nanostructured bismuth oxide on nickel foam with outstanding electrochemical behavior for supercapacitor application. *Mater Today Commun* 36: 106797. https://doi.org/10.1016/j.mtcomm.2023.106797
40. Sudhakar K, Rajeswaran P, Kamatchi T, et al. (2023) Facile one-pot synthesis of porous NiCoP@reduced graphene oxide composite as active electrode material for high energy density asymmetric supercapacitor. *Chem Phys Lett* 826: 140635. https://doi.org/10.1016/j.cplett.2023.140635

41. Gowdhaman A, Kumar SA, Elumalai D, et al. (2023) Ni-MOF derived NiO/Ni/r-GO nanocomposite as a novel electrode material for high-performance asymmetric supercapacitor. *J Energy Storage* 61: 106769. https://doi.org/10.1016/j.est.2023.106769
42. Naveenkumar P, Maniyazagan M, Yesuraj J, et al. (2022) Electrodeposited MnS@$Ni(OH)_2$ core-shell hybrids as an efficient electrode materials for symmetric supercapacitor applications. *Electrochim Acta* 412: 140138. https://doi.org/10.1016/j.electacta.2022.140138
43. Dong L, Zhao W, Liu T, et al. (2022) In situ growth of Ni-Co-S nanosheet arrays on rGO decorated Ni foam toward high-performance supercapacitors. *J Electroanal Chem* 921: 116658. https://doi.org/10.1016/j.jelechem.2022.116658
44. Mane SA, Kashale AA, Kamble GP, et al. (2022) Facile synthesis of flower-like Bi_2O_3 as an efficient electrode for high performance asymmetric supercapacitor. *J Alloys Compd* 926: 166722. https://doi.org/10.1016/j.jallcom.2022.166722
45. Guo W, Lian X, Tian Y, et al. (2021) Facile fabrication 1D/2D/3D Co_3O_4 nanostructure in hydrothermal synthesis for enhanced supercapacitor performance. *J Energy Storage* 38: 102586. https://doi.org/10.1016/j.est.2021.102586
46. Al-Harbi MY, Abdel-Daiem AM, Shalaan E (2023) Self-supporting electrodes obtained by electrochemical dealloying of Zr-based metallic glass alloys for energy storage applications. *J Mater Sci Mater Electron* 34: 1358. http://dx.doi.org/10.1007/s10854-023-10750-x
47. Chang BY (2020) Conversion of a constant phase element to an equivalent capacitor. *J Electrochem Sci Technol* 11: 318–321. https://doi.org/10.33961/jecst.2020.00815
48. Jorcin JB, Orazem ME, Pébère N, et al. (2006) CPE analysis by local electrochemical impedance spectroscopy. *Electrochim Acta* 51: 1473–1479. https://doi.org/10.1016/j.electacta.2005.02.128
49. Li X, Zhou L, Zhao S, et al. (2023) Reduced graphite oxide wrapped ZnO-SnO_2 hollow nanospheres with as anodes for hybrid high energy density supercapacitors. *Diam Relat Mater* 136: 110076. https://doi.org/10.1016/j.diamond.2023.110076
50. Suganya S, Alam MM, Kousi F, et al. (2023) Facile one-pot synthesis of ternary Ni-Mn-Zn oxide nanocomposites for high-performance hybrid supercapacitors. *J Energy Storage* 71: 108176. https://doi.org/10.1016/j.est.2023.108176

AIMS Press